2-1-2016

# Analysis of Kelvin-Helmholtz Instabilities Developing from Oblique Shock Interaction with a Heavy Gas Column
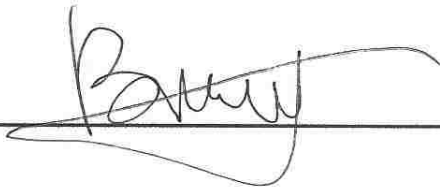
Patrick Wayne

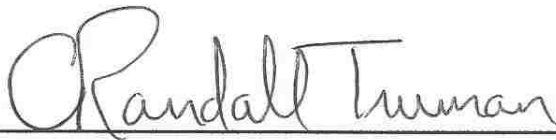Patrick John Wayne

_Candidate_

Mechanical Engineering

_Department_

This thesis is approved, and it is acceptable in quality and form for publication:

_Approved by the Dissertation Committee:_

Professor Peter Vorobieff, Chairperson

Professor C. Randall Truman, Member

Professor Andrea Mammoli, Member

# Analysis of Kelvin-Helmholtz Instabilities Developing from Oblique Shock Interaction with a Heavy Gas Column

by

**Patrick John Wayne**

B. S., Mechanical Engineering, 2012

THESIS

Submitted in Partial Fulfillment of the
Requirements for the Degree of

Master of Science
Mechanical Engineering

The University of New Mexico

Albuquerque, New Mexico

December, 2015

# Acknowledgments

I would first like to thank my advisor, Dr. Peter Vorobieff, who gave me the opportunity to study and research shock-driven instabilities, and who has taught me so much in the short time I've been at UNM. Secondly, I would like to thank Dr. C Randall Truman who has helped me in nearly every aspect of my student career here at UNM. Thank you both for everything you have done.

I would also like to thank my fellow graduate and undergraduate students, Maj. Dell Olmstead (USAF), Clint Corbin, Dylan Simons, and Daniel Davis. Not only for their hard work and dedication in the shock tube lab, but also for their friendship over the last few years.

Most of all, I would also like to thank my family, who has constantly supported me for the past seven years. Without their help and love, I would not be here today. I cannot thank them enough.

# Analysis of Kelvin-Helmholtz Instabilities Developing from Oblique Shock Interaction with a Heavy Gas Column

by

## Patrick John Wayne

B. S., Mechanical Engineering, 2012

M.S., Mechanical Engineering, University of New Mexico, 2015

## Abstract

This thesis presents an experimental study of instabilities developing from oblique shock wave interaction with a heavy gas column. For these experiments, the gas column consists of pure sulfur hexafluoride infused with $\approx$11% acetone gas by mass. A misalignment of the pressure and density gradients (from the shock wave) results in three-dimensional vorticity deposition on the gaseous interface. This is the main mechanism responsible for the formation of traditional Richtmyer-Meshkov instabilities (RMI). Other instabilities develop along the interface due to shear between the injected material and the post-shock air (moving at piston velocity behind the column). These instabilities present on the leading (with respect to the shock) and trailing edges of the column. On the leading edge, small perturbations are amplified by shear at the interface. This leads to the development of full billows, or "cat's eye" vortices, physically indistinguishable from Kelvin-Helmholtz instabilities (KHI). Certain characteristics of the KHI, such as initial instability growth rate and wavelength $\lambda$, depend on several factors including the Mach number of the shock wave, the shock tube angle of inclination $\theta$, and the post-shock compressed size of the column.

# Contents

*Contents*

# List of Figures

# List of Tables

# Chapter 1

# Introduction

Several hydrodynamic instabilities have been discovered and analyzed over the past two centuries. An important and relatively recent discovery is the well-known Richtmyer - Meshkov instability, or RMI. This instability was theoretically described by R.D. Richtmyer in 1954 [4] and its existence was confirmed experimentally by E.E. Meshkov several years later [5]. RMI develops when an interface between two fluids of different density is impulsively accelerated. This acceleration can be the result of an impulsive body force, or due to a passing shock wave [6]. A misalignment of the pressure and density gradients results in three-dimensional vorticity deposition along the interface, causing the formation of a perturbation that grows non-linearly with time, which may eventually transition to fully turbulent flow [7]. These instabilities have been observed in many natural and engineering phenomena, from evolution of supernovae remnants to experiments in high energy density physics at the National Ignition Facility (NIF) in Livermore, California. RMI usually develops (or precipitates) in combination with other hydrodynamic instabilities, such as the Kelvin-Helmholtz instability, or KHI. This instability was first described by Hermann von Helmholtz in 1868. He discovered it while studying the problem of acoustics and

analyzing the solutions of Euler's equation for which friction would play a role [8]. Euler's equations are a form of the Navier-Stokes equations describing momentum and continuity of a fluid flow in which viscous forces can be neglected. Helmholtz's studies included the simple case of a 'vortex sheet' - a continuous alignment of rectilinear vortices - and found it to be equivalent to a tangential discontinuity of the fluid velocity across the sheet [8]. Any perturbations along the interface (tangential discontinuity) between two fluids would [eventually] grow and roll up spirally [8], provided there was sufficient initial perturbation along the interface. Helmholtz postulated this type of instability was similar to one induced by wind blowing across the sea [9]. He also posited that for short enough wavelengths, if surface tension is ignored, two fluids in parallel motion with different velocities will yield an interface that is unstable for all speeds [9].

Inspired by Helmholtz's famous paper "Über Integrale der hydrodynamischen Gleichungen, welche den Wirbelbewegungen entsprechen" [10] (loosely translated "On integrals of the Hydrodynamic equations, which Express Vortex-motion"), the chair of natural philosophy (later called physics) at the University of Glasgow, Sir William Thomson, Baron Kelvin of Largs [11], began studying the flow properties and characteristics of vortex formation. Thomson verified and expanded on the theories of surface waves and vortex roll-up presented by Helmholtz. His collaboration with Helmholtz led to the naming of the now well-known Kelvin-Helmholtz instability, which describes the evolution and morphology of waves generated by shear-driven flow. Although study of KHI began over a century ago with Helmholtz and Thomson, their mathematical and physical descriptions of waves generated in shearing flows apply to an increasing amount of engineering problems and research interests.

Recent experiments conducted in the shock tube facility at the University of New Mexico (UNM) focus mainly on planar or oblique shock wave interactions with a column of heavy gas. In the experiments described here, the column of heavy gas,

consisting of sulfur-hexafluoride ($SF_6$) infused with acetone tracer, is impulsively accelerated by an oblique shock wave. Planar laser induced fluorescence (PLIF) images of the shock-accelerated gas column do reveal the expected evolution of RMI. However, the images also reveal evolution of three-dimensional (3D) small-scale features, morphologically identical to Kelvin-Helmholtz instabilities [2]. As their evolution begins, small periodic perturbations appear along the upstream side of the gaseous interface. Fueled by shear along the interface, the instabilities grow with time into full "cat's eye" [12] vortices, or billows [13], that roll down the entire vertical length of the gas column. At later times, these spiraling instabilities merge with consecutive neighboring vortices and promote mixing, which precipitates transition to turbulence.

## 1.1   Motivation

Earlier research in the shock tube facility at UNM focused on visualization and characterization of hydrodynamic instabilities resulting from shock wave interaction with a heavy gas column, specifically in flows with non-uniform droplet seeding [7] [14] [15] [16]. The initial conditions in these cases consisted of a 6.25 mm diameter column of either sulfur-hexafluoride ($SF_6$), or air, each seeded with glycol fog particles. It was believed that the particles, although relatively large in size and mass compared to $SF_6$ molecules, would correctly follow the material of the shock-accelerated column. In the case of $SF_6$/fog, the glycol droplets did follow the large-scale structures indicative of RMI (counter-rotating vortices). However, many other flow features, such as spikes, bubbles, and KHI could not be visualized in the flow. Simulations using the Eulerian hydrocode SHAMRC (Second-order Hydrodynamic Automatic Mesh Refinement Code) revealed several such features and characteristics of the shock-accelerated column that were difficult to resolve in experiments [17] using glycol fog as a tracer. Figure  1.1 is a comparison between actual experiments using glycol fog

as a tracer, numerical simulations in SHAMRC of pure $SF_6$ initial conditions, and simulations in SHAMRC in which initial particle distribution and $SF_6$ concentration is taken into account, for early times (after shock impact) at Mach $= 1.67$ [1]. Notice that features present in numerics (spike and bunny ears) are not revealed by glycol tracer particles, suggesting that glycol fog (or other particle/droplet tracer) has serious limitations in visualization of shock-driven flows, especially for Mach numbers above 1.5 [18].
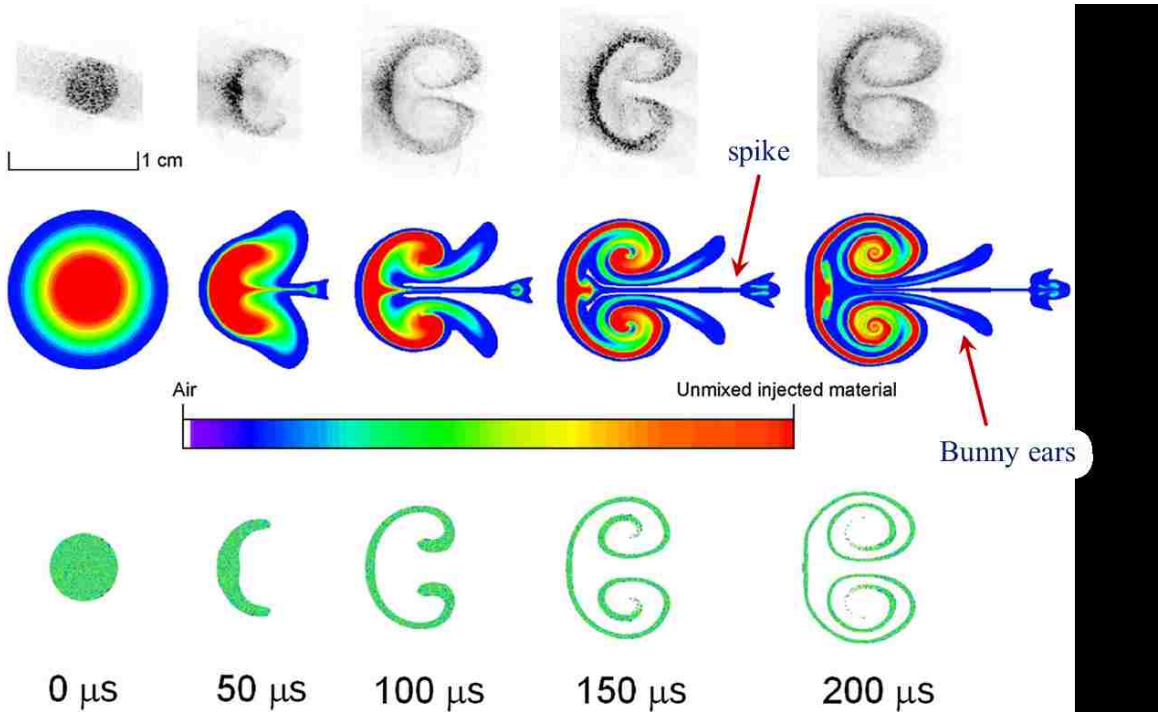


Figure 1.1: Comparison of experimental images (top) using glycol fog as a tracer, density contours generated by SHAMRC (middle) for pure $SF_6$ initial conditions, and particle distributions generated by SHAMRC with initial particle distribution taking the difference between $SF_6$ concentration and particle concentration into account [1].

These realizations led to planar laser-induced fluorescence imaging (PLIF) of the heavy gas column, specifically with acetone gas. PLIF is a non-intrusive measurement technique that provides two-dimensional distributions of a large range of flow field

parameters [19]. PLIF has been successfully used to measure the respective densities of working fluids (gases and liquids alike), fluctuations in velocity, and pressure in the flow field. Acetone is an ideal candidate for PLIF measurements because of its linear relationship between the fluorescence intensity and laser power in an isobaric and isothermal environment [19] [20], but also because of its relatively low vapor pressure at room temperature ( 20° C) [21]. Acetone absorbs [light] in the range of 225 nm to 320 nm wavelength (UV), and emits in the range of 350 nm to 550 nm [19]. The important thing to note about acetone fluorescence is that the absorption and emission spectrum do not overlap. This is an ideal condition as it is easy to filter scattered light from the imaging platform. In addition, acetone is inexpensive and relatively safe to work with.

The first experiments conducted with acetone-infused initial conditions concentrated on planar normal shock interaction with a column of sulfur-hexafluoride ($SF_6$). Preliminary data were encouraging as the images corroborated the numerical simulations performed in SHAMRC [17]. Figure 1.2 is a collection of images for three Mach numbers, M = 1.4, 1.8 and 2.1. The four exposures corresponding to each respective Mach number were obtained in *the same experiment*. UV and visible light laser pulses were staggered to visualize flow features and instabilities using glycol fog particles and acetone gas. Glycol fog droplets do follow large-scale features of RMI, such as the counter-rotating vortex pair (CRVP). However, PLIF visualization of the same experiment(s) resolves features only seen in numerical simulations [1].

Invigorated by the wealth of new, unseen features in the flow, the shock tube group at UNM began experiments studying oblique shock interactions with a column of acetone-infused $SF_6$. Vertical plane images of the shock-accelerated column revealed small perturbations developing on the air/$SF_6$ interface that rolled down the entire length of the column. These perturbations evolved, following the traditional morphology of Kelvin-Helmholtz instabilities and subsequently mixing and transi-
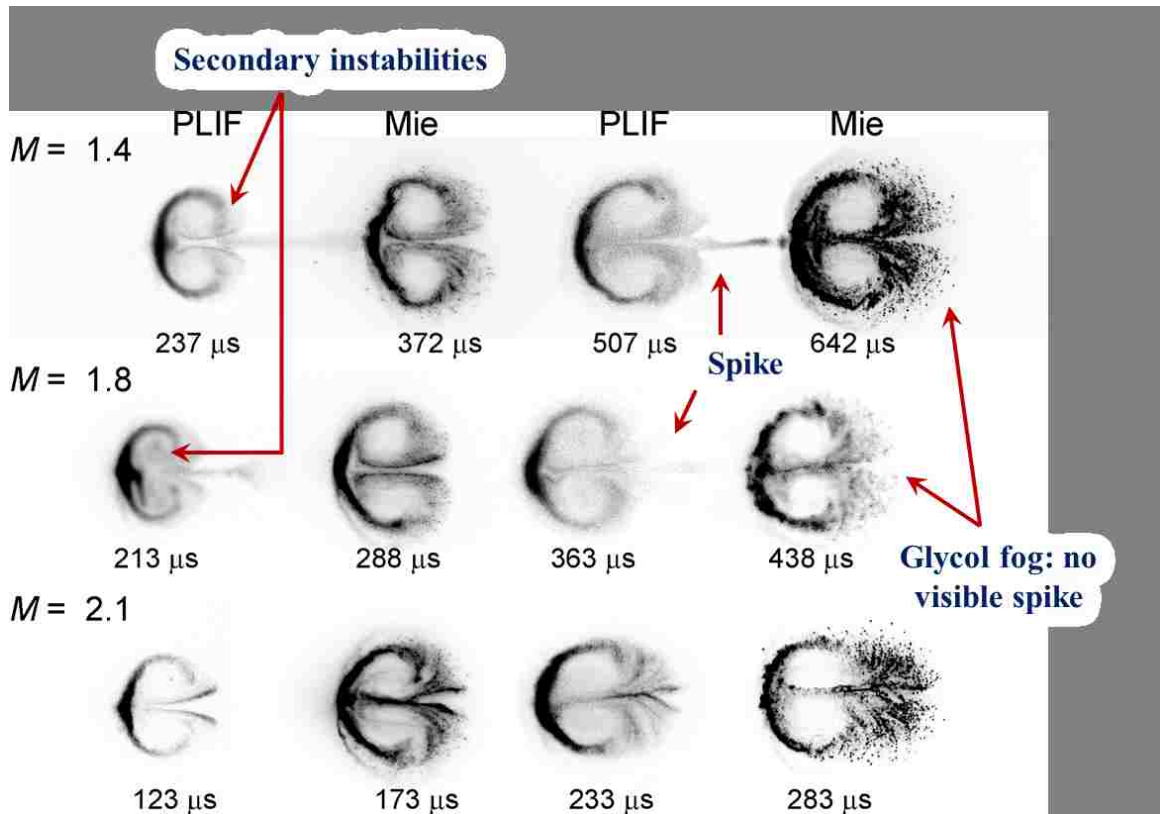
Figure 1.2: Collection of experiments at three different Mach numbers; 1.4, 1.8, and 2.1. Secondary features within the cores of the main counter-rotating vortex pair (CRVP) are visible in PLIF exposures, but remain unseen in exposures with Mie scattering. This raised interest in pure PLIF visualizations of shock-accelerated flow[1].

tioning to fully turbulent flow. It was apparent that these new data required further investigation and scrutiny of the instabilities to fully describe three-dimensional dynamics of the gas column. This thesis focuses on these small-scale Kelvin-Helmholtz instabilities, including theory on how they develop in RMI-dominated flow, a description of how the data were analyzed, and a detailed description of their periodic behavior, with respect to Mach number and the initial angle between the gas column and the plane of the shock.

# Chapter 2

# Experimental Setup

The Shock Tube Facility at UNM is used to study planar and oblique shock interactions with gaseous density interfaces and multiphase flows [7]. The shock tube is unique in one important way. It can operate in a horizontal position, or be inclined to any angle $\theta$ between 0° and 45° above horizontal. Figure 2.1 is an image of the shock tube, inclined to $\theta = 20°$ above horizontal. The tube itself consists of four main sections: the driver, driven, test, and runoff sections. With the exception of the acrylic viewing window on the test section, the shock tube is made entirely out of T6061 aircraft aluminum. Under normal operation, the driver section is pressurized with helium to a predetermined pressure (depending on the desired Mach number of the experiment). A diaphragm separating the driver and driven sections is used to maintain pressure within the driver until it is ready to fire. The type and thickness of the diaphragm depends on the Mach number; either 100 lb. high-gloss photo paper (used for Mach < 1.2), or thin-film polyester (Mach ≥ 1.2). Table 2 lists the various diaphragm materials and target pressure (psi) within the driver section as a function of Mach number. Once the target pressure has been reached, a puncture rod, tipped with a broadhead arrow tip from a commercially available

Figure 2.1: Picture of the shock tube facility at UNM. The shock tube itself is inclined to a 20° angle above horizontal. The main sections of the tube are, from left to right, the driver, driven, test, and runoff sections, respectively. The image shown here is mirrored to retain left-to-right flow direction.

Table 2.1: Diaphragm thickness and driver pressure according to Mach number [3].

| Mach | Type of Film | Thickness (mm) | Driver Pressure (psi) |
|---|---|---|---|
| 1.13 | 100lb Photo Paper | 0.127 | 8 |
| 1.45 | 0.003" Polyester | 0.0762 | 55 |
| 1.70 | 0.005" Polyester | 0.127 | 95 |
| 2.00 | 0.010" Polyester | 0.254 | 195 |

hunting arrow, is driven into the diaphragm, rupturing the material and releasing a planar normal shock down the length of the shock tube and into the test section. Two high-frequency pressure transducers, located 2.60 meters apart on the driven section record the pressure pulse of the shock wave as it propagates downstream. This information is displayed, stored, and is used to trigger the diagnostics (laser and camera) and verify the velocity of the shock: $V_s = 2.60$ m/$\Delta t$, where $V_s$ is the velocity of the shock, and $\Delta t$ is the time between pressure pulses [2]. The value 2.60 m is the distance between the pressure transducers on top of the driven section of the shock tube. This information can then be used to calculate the Mach number as $M = V_s/a$, where $a =$ the speed of sound in air at room temperature and pressure. Average room temperature and pressure for Albuquerque, NM ($\approx$5,000 ft elevation) is 22° C and 84 kPa. The inclined angle of the shock tube, in addition to the gravity-driven initial conditions (injected vertically into the test section and stabilized by a co-flow of air), result in oblique shock interaction between the shock wave and the density interface.

The shock-accelerated column of heavy gas is illuminated by two sets of Neodymium doped Ytrium Aluminum Garnet (Nd:YAG) frequency-quadrupled ultraviolet (UV) lasers. A New Wave Research Gemini 200 UV laser was used in experiments prior to December 2014. A Quantel Evergreen 200 was used in experiments after December 2014. Both are double-pulsed (266 nm wavelength) lasers with pulse widths $\leq$ 10 ns. The UV laser beam is formed into a 1 mm thick sheet by passing the beam through a combination of cylindrical and spherical lenses [22]. Multiple beam lengths, from 1 cm to 5 cm, are accomplished through cylindrical lenses with varying focal lengths. Two imaging planes can be illuminated by the lasers, depending on the rotation of the cylindrical lens: either vertical, or centerline plane. Figure 2.2 illustrates each of these planes and provides dimensions of the test section's inner walls. For the purposes discussed in this paper, only images of the vertical plane are analyzed.
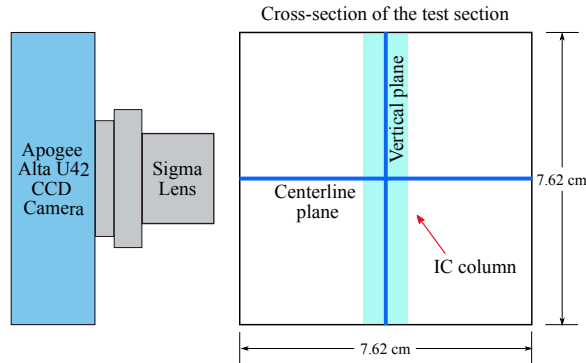
Figure 2.2: Cross-section of the test section, showing both imaging planes with respect to the camera lens. Only images of the vertical plane were analyzed.

Initial conditions (ICs) for the experiments described here, consist of a 6.25 mm diameter column of sulfur-hexafluoride ($SF_6$), infused with acetone gas. The $SF_6$, initially contained in a large compressed gas cylinder, is slowly injected through a small-diameter pipette, into a sealed flask of pure liquid acetone. A simple wooden air diffuser (used in aquariums) on the end of the pipette creates a steady stream of small bubbles of pure $SF_6$ that rise through the liquid acetone. In the process, $SF_6$ becomes infused with acetone before being injected into the test section. Figure 2.3 is an image showing the entire injection assembly. A steady, laminar jet of $SF_6$ is maintained through the use of a flow straightener and co-flow of air. The micrometer adjustment assembly depicted in Figure 2.3 is used to ensure the column remains centered with respect to the exit hole on the bottom of the test section. Velocities of the initial conditions and co-flow of air are about 1.0 m/s and 1.2 m/s, respectively.

Some experiments conducted at the shock tube facility focused on effects of Atwood number variation on the development and morphology of the shock-accelerated column. The Atwood number is a dimensionless density ratio

$$A = \frac{\rho_1 - \rho_2}{\rho_1 + \rho_2} \tag{2.1}$$
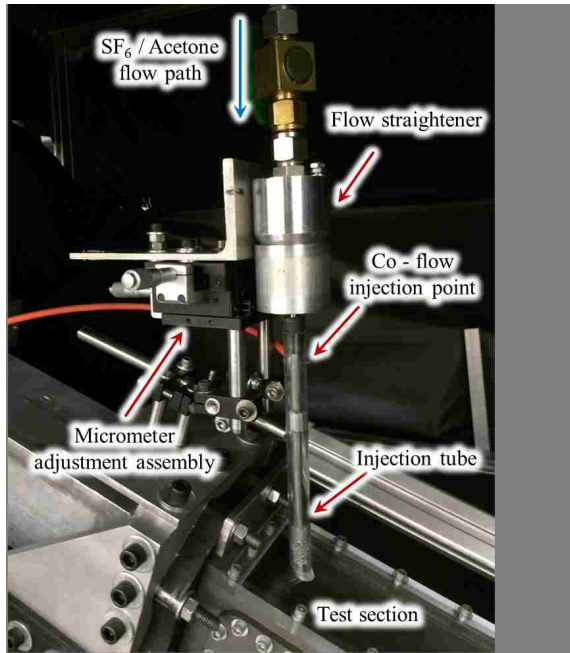
Figure 2.3: Image of the injector assembly, showing the flow path of the initial conditions. The ICs are first injected into a flow straightener before entering the injection tube, stabilized by a co-flow of air. This ensures the column of heavy gas remains a laminar jet through the test section. A micrometer adjustment assembly was added as a method of centering the jet with the exit hole on the bottom of the test section.

where $\rho_1$ and $\rho_2$ correspond to the density of the initial conditions (heavy gas) and the density of air (light gas), respectively. Variations in Atwood number are achieved through partial pressure calculations with $SF_6$ and nitrogen. For example, an Atwood number of 0.499 corresponded to a total pressure in the compressed gas cylinder of $P_{total} = 2497$ kPa (gage), with the total gage pressure of $SF_6$ as $P_{SF6} = 296.5$ kPa and the total gage pressure of nitrogen as $P_{N2} = P_{total} - P_{SF6} = 2201$ kPa. One variable that needed to be taken into account when calculating partial pressures is the liquid-vapor critical point of $SF_6$, which is approximately 3758 kPa at 45.57°C [23]. Pressures above this limit would initiate phase change of the $SF_6$ in the bottle from a gas into a liquid. Therefore, for continuity and safety concerns, the pressure

in each tank of initial conditions (regardless of Atwood number) are kept well below 3,500 kPa.
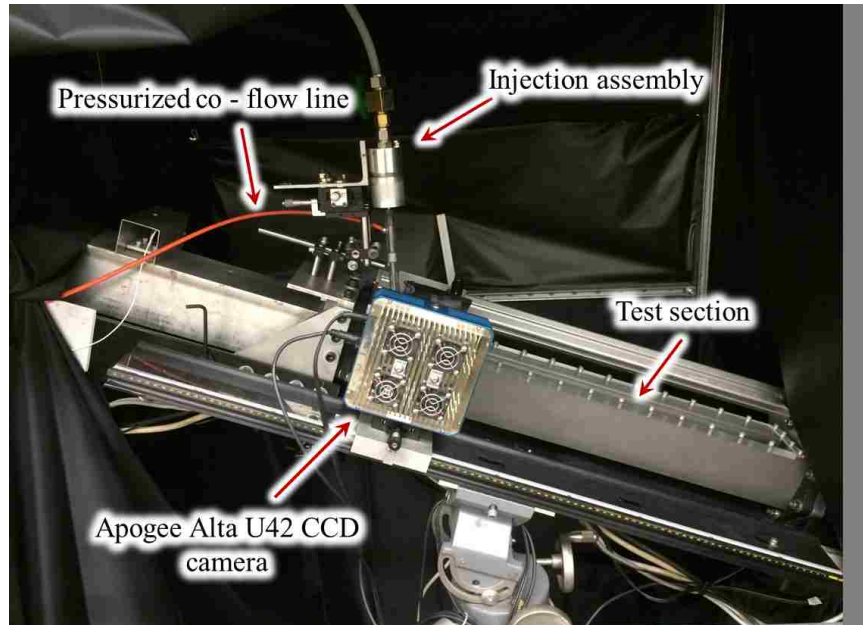


Figure 2.4: Image of the Apogee Alta U42 astronomy camera, parallel with the test section. This picture shows the test section setup for collecting centerline plane dynamic images. A mirror placed on a rail above the top acrylic wall of the test section allowed imaging of the centerline plane. As with Fig. 2.1, the image here is mirrored to retain left-to-right flow direction.

Three different Atwood numbers were chosen for comparison: $A = 0.67$ (which corresponded to pure $SF_6$/air), along with $A = 0.50$, and $A = 0.25$. The percent concentration of acetone in the initial conditions was calculated as approximately 10% [24]. It is important to note that this concentration is not taken into account in any Atwood number calculations. As a result, the actual Atwood number of these experiments is less than the nominal value.

Time-resolved images of the shock-accelerated heavy gas column are obtained using a single-frame Apogee Alta U42 monochrome CCD (charge-couple device) astronomy camera. Exposures are timed to coincide with laser pulses according to the

desired downstream position of the dynamic image. The camera itself is mounted on an aluminum optical rail, aligned parallel with the test section, as seen in Figure 2.4. The camera/rail assembly is mounted on a steel pier with a large tripod head, allowing alignment of the camera on three axes of rotation, plus vertical adjustment. The clear acrylic window of the test section allows unobstructed views of the shocked column as it propagates downstream. A blackout curtain, made by ThorLabs, Inc., is used to minimize noise in every exposure. However, background images with the same exposure time as the dynamic images are always taken prior to each experiment. If needed, background images can be subtracted from the dynamic frames to further minimize noise and reduce light scatter from the lasers in the test section (light scatter from the laser sheet hitting the aluminum sides of the test section and/or exit hole for the column of heavy gas).

Four representative Mach numbers were chosen for the experiments; M = 1.13, M = 1.40, M = 1.70, and M = 2.00. The Mach number for each experiment varied by no more than 0.50% from the nominal value [2]. For a shock tube inclination angle of $\theta = 30°$, up to 20 images per Mach number were used to produce results. However, due to limited time, only a few images per Mach number were obtained for $\theta = 20°$ inclination. The next section expands on history and theory associated with Richtmyer-Meshkov and Kelvin-Helmholtz instabilities, including physical descriptions of each, and a hypothesis as to why KHI develop along the upstream and downstream sides of the column, given there are no resolvable perturbations in the initial conditions.

# Chapter 3

# Kelvin-Helmholtz Instabilities

Earlier in history, particularly during the 17th and 18th centuries, theoretical and experimental approaches to fluid motion evolved on parallel, but separate paths. *Hydrodynamics* was the term associated with the theoretical or mathematical study of idealized, frictionless fluid behavior, with the term *hydraulics* being used to describe the applied or experimental aspects of real fluid behavior, particularly the behavior of water [25]. Hydrodynamics is now defined as a branch of physics that deals with the motion of fluids and the forces acting on solid bodies immersed in fluid and in motion relative to them [26]. The stability of these hydrodynamic flows is of practical importance to nearly every applied discipline dealing with fluid flow, such as aeronautics and astronautics, hydraulics, astrophysics, and oceanography. Of the two types of hydrodynamic instabilities talked about previously, only one is due to impulsive acceleration, the Richtmyer-Meshkov instability (RMI). Depending on the parameters of the experiment and/or initial conditions, other hydrodynamic instabilities may evolve in conjunction with RMI, or be driven by it. However, the main field quantity most relevant for RMI and subsequent secondary instabilities (such as KHI) is vorticity.

## 3.1 Vorticity

Vorticity is defined as the curl of the velocity vector, or $\vec{\omega} = \vec{\nabla} \times \vec{u}$, where $\vec{\omega}$ is the vorticity vector and $\vec{u}$ is the velocity vector [27] [28] [29]. In simple terms, the angular velocity of a fluid element is equal to half of the vorticity [28]. For two-dimensional, viscous, compressible flows, the vorticity equation is given as

$$\frac{D\vec{\omega}}{Dt} = \vec{\omega} \cdot \vec{\nabla}\vec{u} + \vec{u}\vec{\nabla}^2\vec{\omega} + \left(\frac{1}{\rho^2}\vec{\nabla}\rho \times \vec{\nabla}p\right) \tag{3.1}$$

where $\frac{D\vec{\omega}}{Dt}$ is the material derivative of $\vec{\omega}$, $\rho$ is the density of the fluid, and $p$ is the pressure. The first term on the right hand side of Equation 3.1 represents the generation of vorticity due to a velocity gradient or vortex stretching [7]. The second term represents vorticity generation due to compressibility and the third term is the baroclinic vorticity term [7]. For the experiments described here, there is no initial vorticity present in the flow, therefore the first two terms may be canceled leaving only the baroclinic term.

$$\frac{D\vec{\omega}}{Dt} = \left(\frac{1}{\rho^2}\vec{\nabla}\rho \times \vec{\nabla}p\right) \tag{3.2}$$

The misalignment of the pressure gradient across the shock front and the density gradient(s) in the column of heavy gas results in three-dimensional vorticity deposition [2] on the gas-gas interface. In the centerline plane (Figure 3.1a., top right), this deposition results in the formation of a counter-rotating vortex pair, indicative of RMI. In the vertical plane (Figure 3.1a., bottom right) vortex sheets form on the upstream and downstream sides of the column [2], which result in the formation of a shear layer on each interface.

After shock impact, the light gas (air in our experiment), which is moving at piston velocity $\Delta V$ (Figure 3.1b)) will impact the leading edge of the column. Although most of this air will circumvent the gas column and travel around it, a component of that air will travel down the leading edge, resulting in a velocity difference across
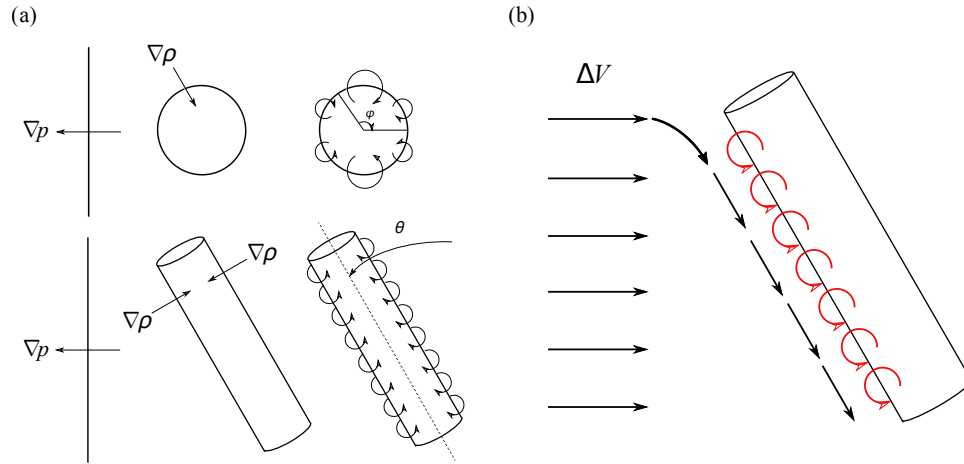
Figure 3.1: a) Schematic depicting baroclinic vorticity deposition on the heavy gas column by the shock wave for both centerline and vertical planes. b) Sketch of air impacting the gas column and traveling down its vertical length, resulting in a velocity difference between the air (which is moving at piston velocity $\Delta V$) and the column of heavy gas [2].

that interface. Any perturbations present in the column will be amplified by this velocity difference, resulting in the formation of co-rotating vortices, characteristic of Kelvin-Helmholtz instabilities.

The amplitude and corresponding wavelength of the KHI are dependent on the amplitude of the initial perturbation and magnitude of the velocity difference across the interface. It can also be interpreted as follows: the cross product of $\vec{\nabla}\rho$ and $\vec{\nabla}p$ is nonzero, leading to deposition of a vortex sheet on the interface - in effect, a shear layer, producing KHI. As the Mach number increases $\vec{\nabla}p$ increases, resulting in stronger vorticity deposition. In fact, it will be shown that the respective wavelength of the KHI for each experiment depends on several factors, including the strength of the shock (baroclinic vorticity), the local Atwood number, and the shock tube's angle of inclination.

## 3.2  Wave Propagation Theory
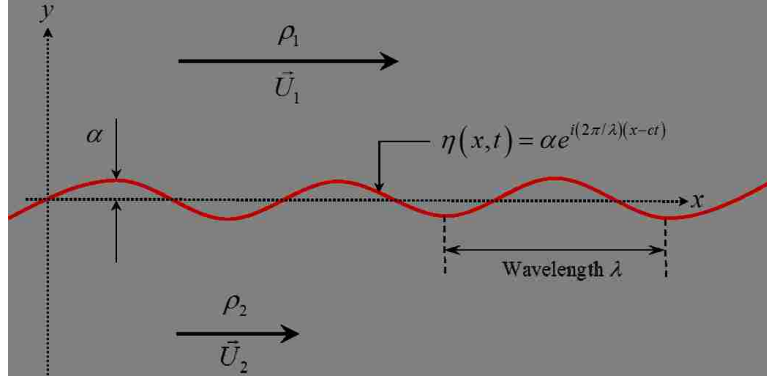


Figure 3.2: Schematic of a two-dimensional, perturbed interface between two fluids. $\vec{U}_1$ and $\rho_1$ correspond to the lighter fluid and $\vec{U}_2$ and $\rho_2$ correspond to the heavier fluid. The wavelength $\lambda$ is measured from peak to peak (in amplitude).

Consider an incompressible, two-dimensional, inviscid fluid flow in which a lighter fluid rests on a heavier fluid, as shown in Figure 3.2, where $\rho_1$ and $\vec{U}_1$ correspond to the density and velocity of the lighter fluid and $\rho_2$ and $\vec{U}_2$ correspond to the density and velocity of the heavier fluid, respectively. Assume a disturbance on the interface between the two fluids is sinusoidal in nature and the equation representing the interface is

$$y = \eta\left(x, t\right) = \alpha e^{i(2\pi/\lambda)(x-ct)} \tag{3.3}$$

where $\alpha$ is the amplitude, $\lambda$ is the wavelength, and $c$ is the complex propagation speed of the wave. It has been shown [27][30] that if $c$ is real, the wave is traveling in the positive $x$-direction with velocity $c$, without growing or decaying. However, if $c$ is imaginary, the wave is either decaying ($c_i$ is negative), or growing ($c_i$ is positive). The system is unstable if $c_i > 0$.

Both flows (upper and lower) are governed by LaPlace's equation, given by

$$\nabla^2 \phi_i = \frac{\partial^2 \phi_i}{\partial^2 x} + \frac{\partial^2 \phi_i}{\partial^2 y} = 0 \tag{3.4}$$

where $\phi_i$ is the velocity potential, and the subscript $i$ is 1 for the upper fluid and 2 for the lower fluid. This equation is second-order in nature, therefore solutions of this equation must also satisfy two boundary conditions for each fluid.

By introducing velocity potentials of the form $\vec{u_i} = U_i e_x + \nabla \phi_i$ and substituting them into the material derivative $D/Dt$, the kinematic boundary condition [27][30] for both sides of the interface is

$$\frac{\partial \phi_i}{\partial y}(x,t) = \frac{\partial \eta}{\partial t}(x,t) + U_i \frac{\partial \eta}{\partial x}(x,t) \tag{3.5}$$

The material derivative $(D/Dt)$ is very useful in analyses involving fluid parameters because it provides the rate at which that parameter changes with time [25]. However, Eqn. (3.5) provides only one boundary condition per fluid for this analysis. One more boundary condition for each fluid is needed. The interface itself can be seen as an instantaneous transition from one velocity to the next. However, the pressure in each fluid (regardless of density) is constant and because the fluids are inviscid, Bernoulli's equation applies. In unperturbed flow where $(\phi = \eta = 0)$, the pressure condition at the interface is

$$B_i = \frac{1}{2}U_i^2 + \frac{p_0}{\rho_i} \tag{3.6}$$

where $B$ is the Bernoulli constant and $p_0$ is the pressure within the fluid [30]. This equation is valid for both fluids because the pressure is constant $(p_0)$ across the interface. Substituting $\vec{u_i}$ in Eqn. (3.6) and neglecting higher order terms in the velocity potential result in

$$\rho_i \frac{\partial \phi_i}{\partial t}(x,t) + \rho_i U_i \frac{\partial \phi_i}{\partial x}(x,t) + \rho_i g \eta(x,t) = constant \tag{3.7}$$

where $g$ is the acceleration due to gravity. The kinematic term $\left(U_i^2/2\right)$ of Eqn. (3.6) is absorbed into the constant on the RHS of Eqn. (3.7)[27]. Eqn. (3.7) provides the last two boundary conditions needed to solve for the wave propagation speed.

Once again, the equation to be satisfied by the velocity potential $\phi_i$ is LaPlace's equation; Eqn. (3.4). Here, the velocities derived from $\phi_i$ should be finite ($\phi_i$=finite) [27]. In the region $y > 0$, $\phi_1$ must satisfy Eqn. (3.4) and in the region $y < 0$, $\phi_2$ must satisfy Eqn. (3.4). The general solution to Eqn. (3.4) that satisfies the finite velocity condition above is given by

$$\phi_i = C_i e^{(2\pi/\lambda)y} e^{i(2\pi/\lambda)(x-ct)} \tag{3.8}$$

where $C_i$ was found to be equal to $i\alpha\,(-c + U_i)$[27]. Substituting this back in to Eqn. (3.8) provides the complete equation for velocity potential in the upper and lower regions of the flow

$$\phi_i\,(x, y, t) = -i\alpha\,(-c + U_i)\,e^{(2\pi/\lambda)y} e^{i(2\pi/\lambda)(x-ct)} \tag{3.9}$$

This solution, when substituted into Eqn. (3.4), satisfies all conditions except the pressure condition, Eqn. (3.7). Expanding out Eqn. (3.7) for the upper and lower fluid and substituting in Eqn. (3.8) for $\phi_i$ yields

$$-\rho_2 \frac{2\pi}{\lambda}\,(c - U_2)^2 + \rho_2 g = -\rho_1 \frac{2\pi}{\lambda}\,(c - U_1)^2 + \rho_1 g \tag{3.10}$$

where $\eta(x, t)$ has been canceled throughout this equation as a nonzero common factor [27]. The end result is an algebraic equation for the wave propagation speed in terms of wavelength, the mean velocity components ($U_i$), the density of the fluids, and acceleration due to gravity. Assuming all quantities in this equation are known except for the complex propagation speed $c$, Eqn. (3.10) can be manipulated into quadratic form. This equation can then be solved for the propagation speed directly

$$c = \frac{\rho_1 U_1 + \rho_2 U_2}{\rho_1 + \rho_2} \pm \sqrt{\left(\frac{\rho_1 U_1 + \rho_2 U_2}{\rho_1 + \rho_2}\right)^2 - \left(\frac{\rho_1 U_1{}^2 + \rho_2 U_2{}^2}{\rho_1 + \rho_2}\right) - \left(\frac{\rho_1 - \rho_2}{\rho_1 + \rho_2}\right)\frac{g\lambda}{2\pi}} \tag{3.11}$$

which is a general dispersion equation for waves on moving fluids of different densities [30]. In order to implement this equation in this analysis of KHI, several factors

need to be considered. For instance, Eqn. (3.11) assumes the flow is incompressible and both fluids are inviscid. In the experiments described here, the flow *is* compressible and the viscosity of each gas may affect the evolution and morphology of the instabilities.

## 3.2.1   The Effects of Viscosity and Gravity

Viscosity modifies the analysis with respect to stability. Equation 3.11 assumes a discontinuity at the interface between the two fluids: an instantaneous transition from one velocity to another. If viscosity is included, the discontinuity in velocities is not possible but the shear layer will extend over a finite thickness instead [30], given that the interface is initially diffuse. Shear instabilities, such as Kelvin-Helmholtz, can be described as the formation of structures which draw kinetic energy out from the flow [31]. Intuition says viscosity tends to stabilize the flow, particularly with respect to small-scale disturbances. However, the opposite is true; the mean flow transfers energy to the disturbances *due* to viscous effects, destabilizing the flow. Inertial effects in our experiments dominate over viscous effects, but viscous effects determine the evolution of the KHI and corresponding turbulent transition.

If viscous effects are to be considered, the wavelength to shear velocity relationship becomes much more complex. The instability can form a cusp, in which case it becomes a Holmboe instability [30], which is composed of a pair of oppositely propagating modes which interact to produce limited mixing of the background density gradient [31]. The physical difference between Holmboe and Kelvin-Helmholtz instabilities are that Holmboe waves grow more slowly than K-H waves, but the net amount of mixing taking place due to the Holmboe waves is greater [13].

Gravitational effects must also be considered when analyzing any fluid flow. For
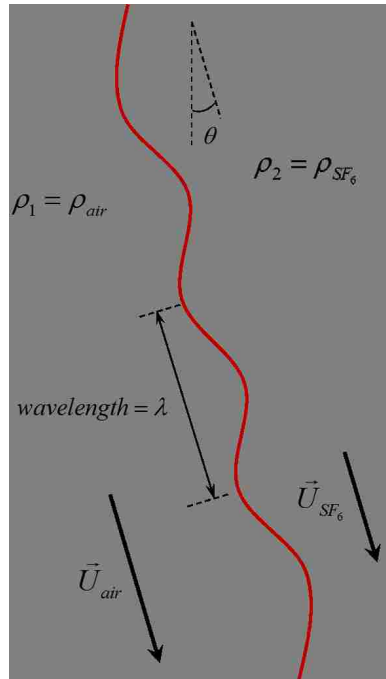
Figure 3.3: Modified schematic of the same perturbed interface as in Fig. 3.2, showing the inclined interface between the column of $SF_6$ and the surrounding air, where $\theta$ is the angle of inclination from vertical. $\vec{U}_{air}$ corresponds to the velocity of the light gas (air) moving down the interface, while $\vec{U}_{SF_6}$ corresponds to the velocity of the heavy gas ($SF_6$). In this schematic, the velocity of the lighter gas is greater than the velocity of the heavy gas.

two-dimensional stably-stratified flows, gravity provides a restorative force, helping to stabilize any perturbations on the fluid interface. However, for experiments described here, gravitational effects may be so small compared with other effects that they can be neglected completely.

Consider a modification to the flow situation depicted in Fig. 3.2 in which the fluid densities are defined as $\rho_{air}$ and $\rho_{SF_6}$. Figure 3.3 is nearly identical to the flow situation in our experiments. Assume the heavy gas, in this case $SF_6$, is moving more slowly than the light gas (air). If we were to consider the time scales (a few microseconds) involved with shock-accelerated flows, then gravitational effects are

essentially nonexistent. Therefore, the gravitational term in Eqn. (3.11) may be omitted yielding

$$c = \frac{\rho_1 U_1 + \rho_2 U_2}{\rho_1 + \rho_2} \pm \sqrt{\left(\frac{\rho_1 U_1 + \rho_2 U_2}{\rho_1 + \rho_2}\right)^2 - \left(\frac{\rho_1 U_1^2 + \rho_2 U_2^2}{\rho_1 + \rho_2}\right)} \qquad (3.12)$$

The interesting thing about Eqn. (3.12) is the complex wave propagation speed does *not* depend on the wavelength ($\lambda$) of the instabilities. The problem with this equation, as far as these experiments are concerned, is that the quantities $U_1$ and $U_2$ are unknown variables and cannot be obtained without direct measurements using image correlation (ICV) or particle image velocimetry (PIV). Granted, there may be some additional modifications needed to fully describe wave propagation along the $SF_6$/air interface. But a basic understanding of wave propagation theory may prove to be useful in analyzing the different features associated with the Kelvin-Helmholtz instabilities seen in these experiments.

# Chapter 4

# Experimental Results

Oblique shock experiments were conducted for two inclination angles: $\alpha = 20°$ and $\alpha = 30°$. Governing parameters for each experiment are the Mach number ($M = V_s/a$), the Atwood number, given by Eqn. (2.1), and non-dimensional time $\tau$

$$\tau = kA\Delta V(t - t_0) \tag{4.1}$$

where $k = 2\pi/d_{ic}$ is the perturbation wavenumber, $d_{ic} = 6.25$ mm is the diameter of the initial conditions, $A$ is the Atwood number, $\Delta V$ is the piston velocity, and $(t - t_0)$ is the time after shock arrival at the center of the heavy gas column [2][7]. Non-dimensional time $\tau$, which is derived from the linear growth theory of RMI [4], is an important parameter because it normalizes the initial instability growth rate for all Mach numbers. Four representative Mach numbers were chosen: $M = 1.13$, $M = 1.45$, $M = 1.70$, and $M = 2.00$. Piston velocities for each Mach number were obtained through an online gas dynamics calculator [32] and are given in Table 4.1.

All images were processed and analyzed separately, within the same area of interest (AOI). Figure 4.1 shows the physical size and location of the AOI for each of the inclination angles. It is important to note that images taken at $\theta = 20°$ are at a

Table 4.1: Piston velocity $\Delta V$ with respect to Mach number

| Mach Number | Piston Velocity (m/s) |
|:-----------:|:---------------------:|
| 1.13 | 70.65 |
| 1.45 | 219.2 |
| 1.70 | 320.6 |
| 2.00 | 432.5 |

much higher resolution and cover a narrower field of view, but the physical size and approximate vertical location of the AOI remain the same.
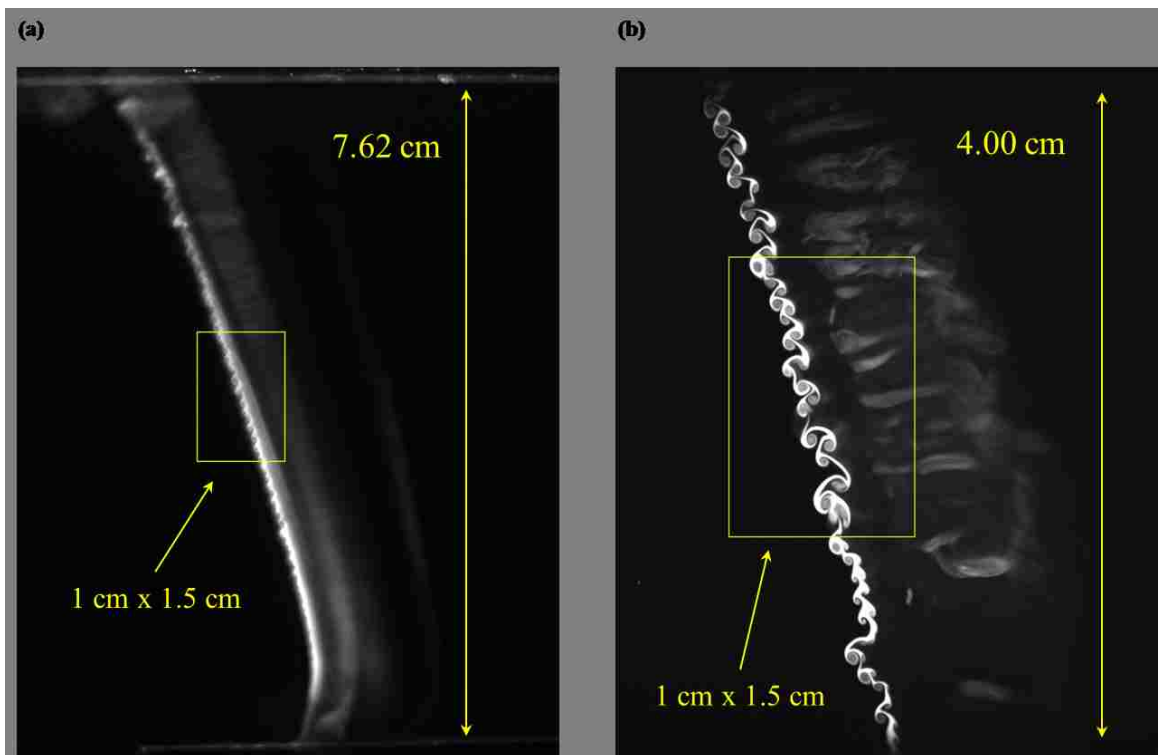


Figure 4.1: Area of interest (AOI) for inclination angles of a. $\theta = 30°$ and b. $\theta = 20°$. The full height of the test section is 7.62 cm. Quantitative and qualitative analysis only applies to features within the area of interest. Flow direction is from left to right [2].

It is important to note that the presence of the Kelvin-Helmholtz waves was not expected because they do not appear in similar experiments of shock wave interaction with a single tilted interface [33][34]. However, their existence should not be surprising. As depicted in Fig. 3.1, air travels down the leading edge of the column, which creates a shear layer on the diffuse air/$SF_6$ interface (both upstream and downstream sides). KHI are shear-driven instabilities that develop on virtually any scale, from large-scale astrophysical phenomena to wind blowing over the surface of a pond. By analyzing the instabilities, it is possible to characterize their behavior and quantify their development. The next two sections examine particular features of Kelvin-Helmholtz instabilities that appear in vertical plane images of the shock-accelerated column, including qualitative aspects and quantitative measurements.

## 4.1   Qualitative Results

Figure 4.2 is a sequence of six images showing temporal evolution of KHI for a $M = 2.00$ shock wave, an angle of inclination $\theta = 30°$, and an Atwood number of 0.42. False colors were used in an effort to resolve the smallest possible features within the area of interest. The color bar on the bottom of the image depicts high density regions as white or yellow, corresponding to pure injected material, then darkening in color down to black, which corresponds to pure, unseeded air.

At $\tau = 25$ (90 $\mu$s), the initial perturbations on the interface are being amplified and begin to form wave-like structures on the leading (upstream) edge of the column. Notice the natural progression of the waves in this images, moving from top to bottom: small perturbations are amplified into larger and larger wave-like structures. At $\tau = 28$ (9 $\mu$s later), the waves are forming along the entire leading edge; growing in both amplitude and wavelength $\lambda$. Wavelength is simply the linear distance between the centers of adjacent vortices (refer to Fig. 4.2 at $\tau = 28$). Also notice the small
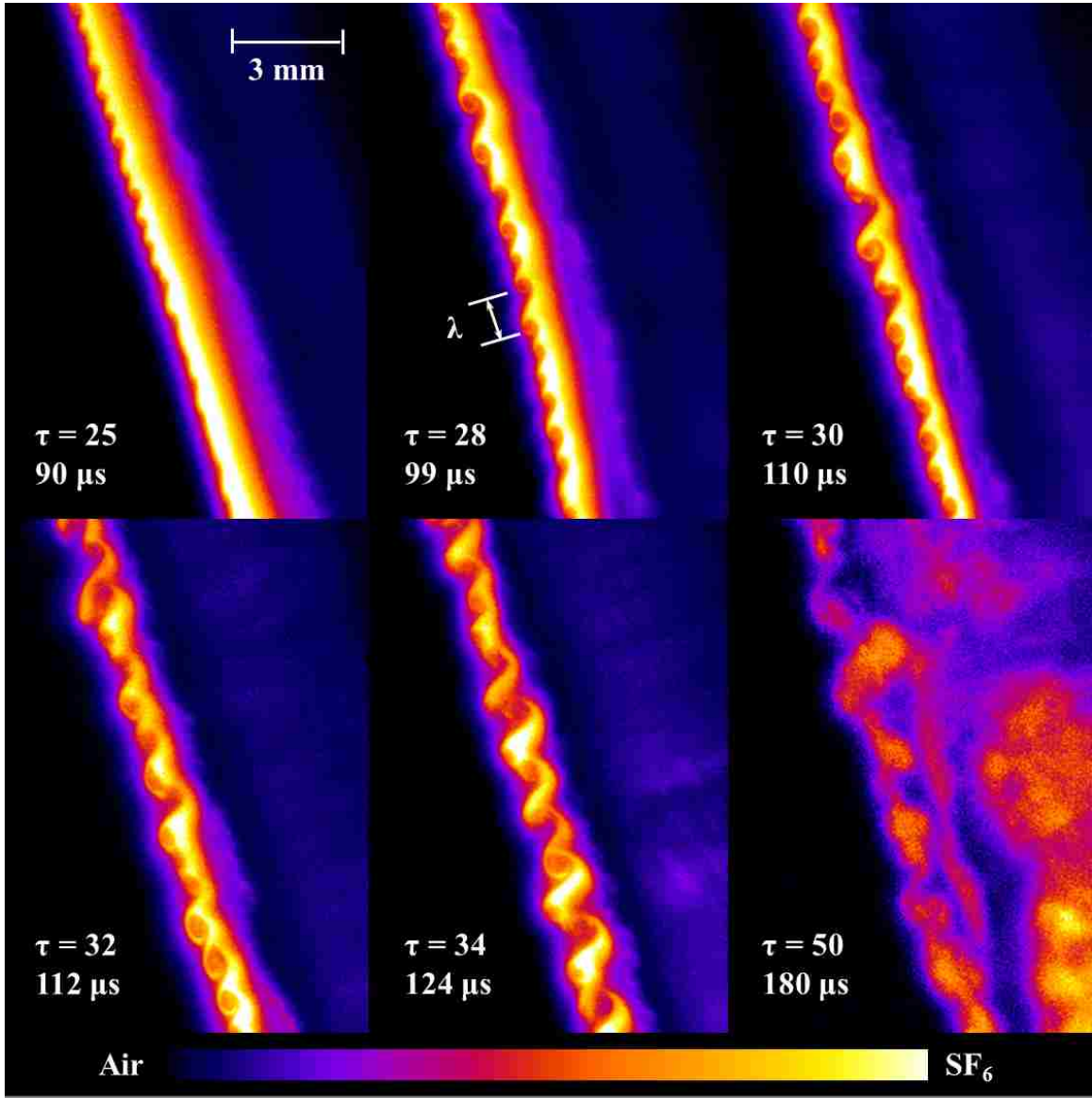
Figure 4.2: Temporal evolution of Kelvin-Helmholtz waves from onset ($\tau = 25$) to turbulent transition ($\tau = 50$) for a Mach 2.00 shock wave, at an inclination angle of $\theta = 30°$, and an Atwood number of 0.42. Flow direction is from left to right. $\tau$ increases from left to right and from top to bottom, respectively.

features on the trailing (downstream) edge of the high density region. This type of "feathering" is normal for these experiments and shows that three-dimensional vorticity is deposited on both sides of the column at shock impact. Shock focusing on the trailing edge of the column is likely responsible for this feature and the reason no KHI develop along that side of the column. The time scale associated with shock focusing is an order of magnitude smaller than the time scale of the KHI on the leading edge of the column. At $\tau = 30$ and 32, the waves grow larger into fully-developed billows or "cat's eye" vortices [12], characteristic of KHI. The feathering on the trailing edge of the high density region is also forming small wave-like structures, although their morphology and growth rate are somewhat different than those on the leading edge of the column. A relatively short time later, at $\tau = 34$, the waves begin to combine and effectively double in wavelength, before transitioning to turbulence at $\tau = 50$. Similar trends were observed for all Mach numbers and inclination angles (including preliminary results at $\theta = 15°$).

Several sets of images were taken at increasing downstream distances for each Mach number and angle $\theta$. Images shown here were chosen based on having fully-developed, resolvable billows along the entire leading edge (within the AOI). Figure 4.3 shows a set of images taken at a 30° angle of inclination. Mach number increases from left to right starting with $M = 1.13$, the lowest possible Mach number for the current experimental configuration. Notice that as the Mach number increases, the amplitude and wavelength of the KHI seem to decrease.

Figure 4.4 shows that a similar trend was found for a 20° angle of inclination; KHI amplitude and wavelength decrease as Mach number increases. However, it is important to note that wavelength measurements for low Mach number ($M = 1.13$) images were difficult to obtain because the Kelvin-Helmholtz waves appeared suddenly (Fig. 4.4 left), the high density interface mixed quickly, and the flow transitioned to turbulence sooner than expected. As a result, measurements of $\lambda$ for
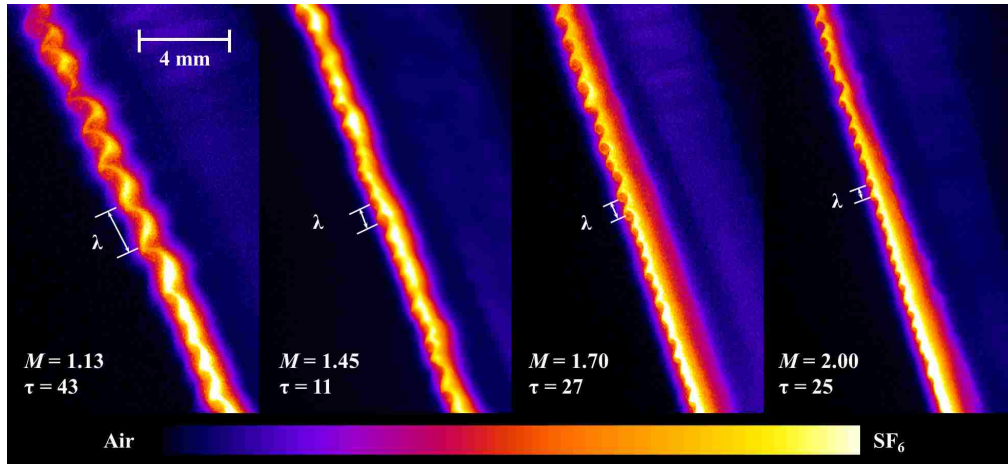
Figure 4.3: Comparison of KHI vortices at four different Mach numbers for a 30°
angle of inclination. Mach number increases from left to right: $M = 1.13$, $M = 1.45$,
$M = 1.70$, and $M = 2.00$.
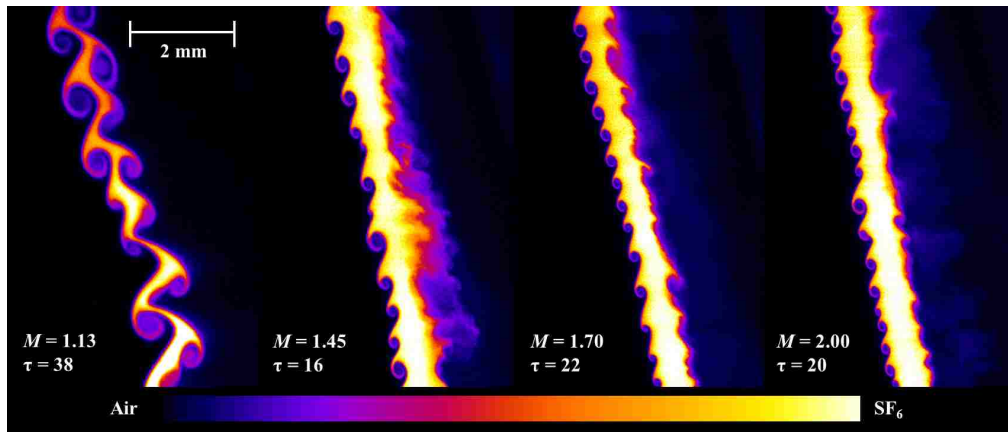


Figure 4.4: Comparison of KHI vortices at four different Mach numbers at a 20°
angle of inclination. Notice the trend is the same as the $\theta = 30°$ case; amplitude and
wavelength decrease as Mach number increases.

$M = 1.13$ images do come with a higher uncertainty, somewhere in the range of 20%, for $\theta = 20°$, and approximately 10% for $\theta = 30°$. However, measurements of $\lambda$ for higher Mach numbers (and both inclination angles) are not as ambiguous and were obtained with a higher degree of accuracy.
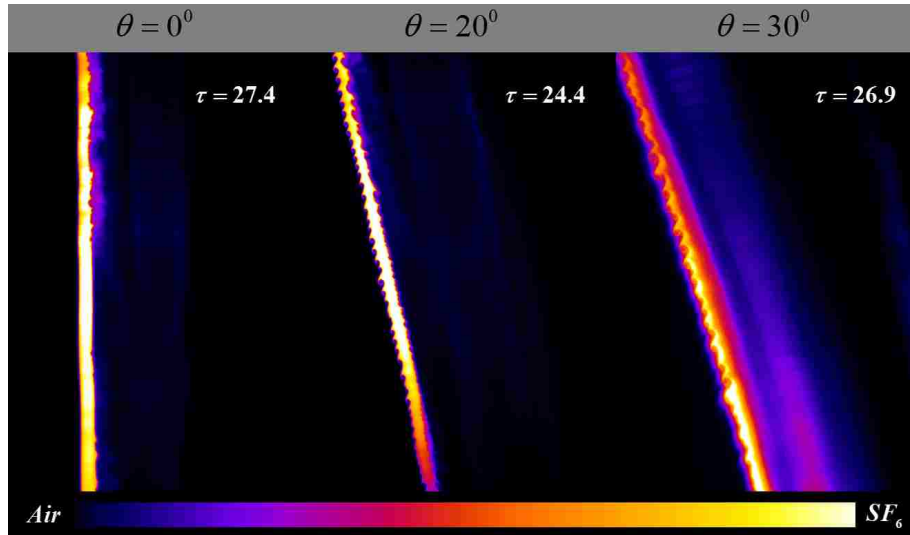


Figure 4.5: Images of three different inclination angles: $\theta = 0°$, $\theta = 20°$, and $\theta = 30°$. Mach number for each image is $M = 1.70$. Images were chosen at the same relative non-dimensional time $\tau$. This ensures matching development of three-dimensional instabilities for each inclination angle.

As experiments into KHI on the diffuse interface continued, another feature of their development became clear: KHI wavelength also depends on the inclination angle $\theta$ of the shock tube. For a horizontal arrangement, where $\theta = 0°$ (Fig. 4.5, left), no instabilities are present on the leading edge of the column. This is expected because no shear layer exists on that edge. However, with increasing inclination angle from horizontal (Fig. 4.5, middle, right), shear velocities begin to develop along the interface and in turn, amplify any initial perturbation along the leading edge. The interesting thing about this is that as $\theta$ increases, the difference in shear velocities decreases. A thorough explanation of this feature, along with theoretical analysis of post-shock behavior will be discussed in the next section.

## 4.2   Quantitative Results

Measurements of wavelength $\lambda$ were taken over 5 consecutive pairs of vortices within the AOI for each image as the average, then sorted according to inclination angle $\theta$ and Mach number. For $\theta = 30°$, up to 17 images per Mach number were used to find $\lambda$. However, due to time and equipment constraints, only a few images per Mach number were used for the $\theta = 20°$ case. Figure 4.6 presents wavelength versus Mach number for (a) $\theta = 30°$ and (b) $\theta = 20°$ inclination angles. Here, wavelength is normalized by $d_{ic}$ (diameter of the initial conditions). The vertical error bars for each graph correspond to $\pm$ one standard deviation in wavelength, also normalized by $d_{ic}$. The horizontal error bars correspond to $\pm$ one standard deviation in Mach number. The curve fit (red line) seen in each graph is a visual aid only, not to be mistaken for predictions of wavelength within that range - $M = 1.13$ to $M = 2.00$.

Notice that wavelength does decrease as the Mach number increases and as the inclination angle $\theta$ decreases. Wavelength according to Mach number for each inclination angle is given in Table 4.2. Wavelength for the $\theta = 30°$ case ranges from about 1.0 mm to 1.6 mm. For the $\theta = 20°$ case, wavelength ranges from about 0.5 mm to 1.1 mm.

Table 4.2: Wavelength $\lambda$ according to Mach number for inclination angles $\theta = 30°$ and $\theta = 20°$, respectively.

| Mach Number | Wavelength $\lambda$ for $\theta = 30°$ | Wavelength $\lambda$ for $\theta = 20°$ |
|---|---|---|
| 1.13 | 1.58 | 1.10 |
| 1.45 | 1.19 | 0.67 |
| 1.70 | 0.99 | 0.57 |
| 2.00 | 0.97 | 0.49 |

(a)

(b)
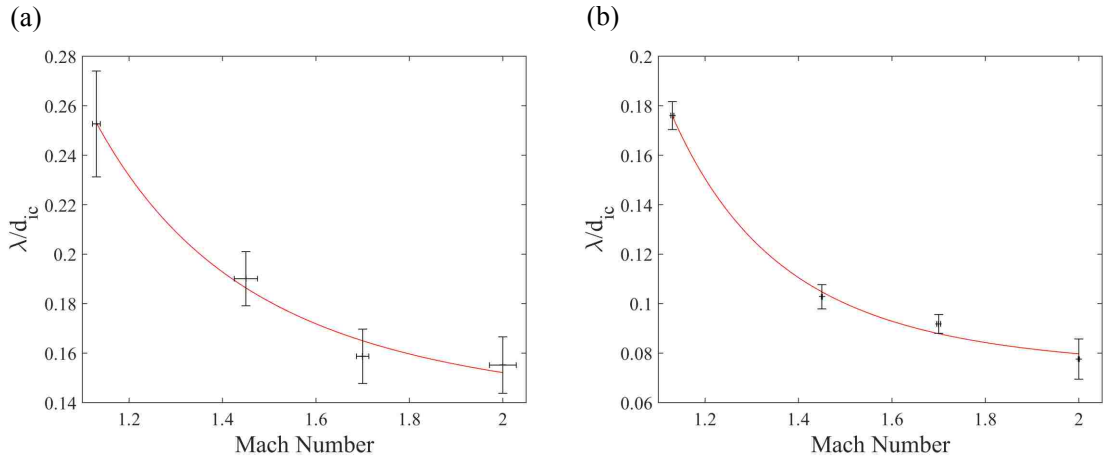


Figure 4.6: Graphs of normalized wavelength versus Mach number for (a) $\theta = 30°$ and (b) $\theta = 20°$ inclination angles. Error bars are normalized standard deviation in wavelength (vertical) and standard deviation in Mach number (horizontal).

## 4.2.1   Theoretical Analysis

The next step in our analysis was to attempt to explain KHI wave behavior using a theoretical approach. The main goal of this analysis is to obtain a solution that would quantify shear velocities on the interface between the column of heavy gas and surrounding air. By knowing the magnitude of these shear velocities, it may be possible to predict wavelengths for a large range of Mach numbers and inclination angles, and use as a basis for programming numerical simulations with similar flow characteristics.

This analytical approach was proposed by Sanjay Kumar, a professor at the Indian Institute of Technology in Kampur, India (IITK). The approach is somewhat complex, but does require a full description to understand how we arrived at our conclusions. Consider a simplified analysis of shock compression on the tilted gas interface, Fig. 4.7. Let the contact point O be the point at which the incident shock impacts the leading edge of the diffuse interface. For a sufficiently small length
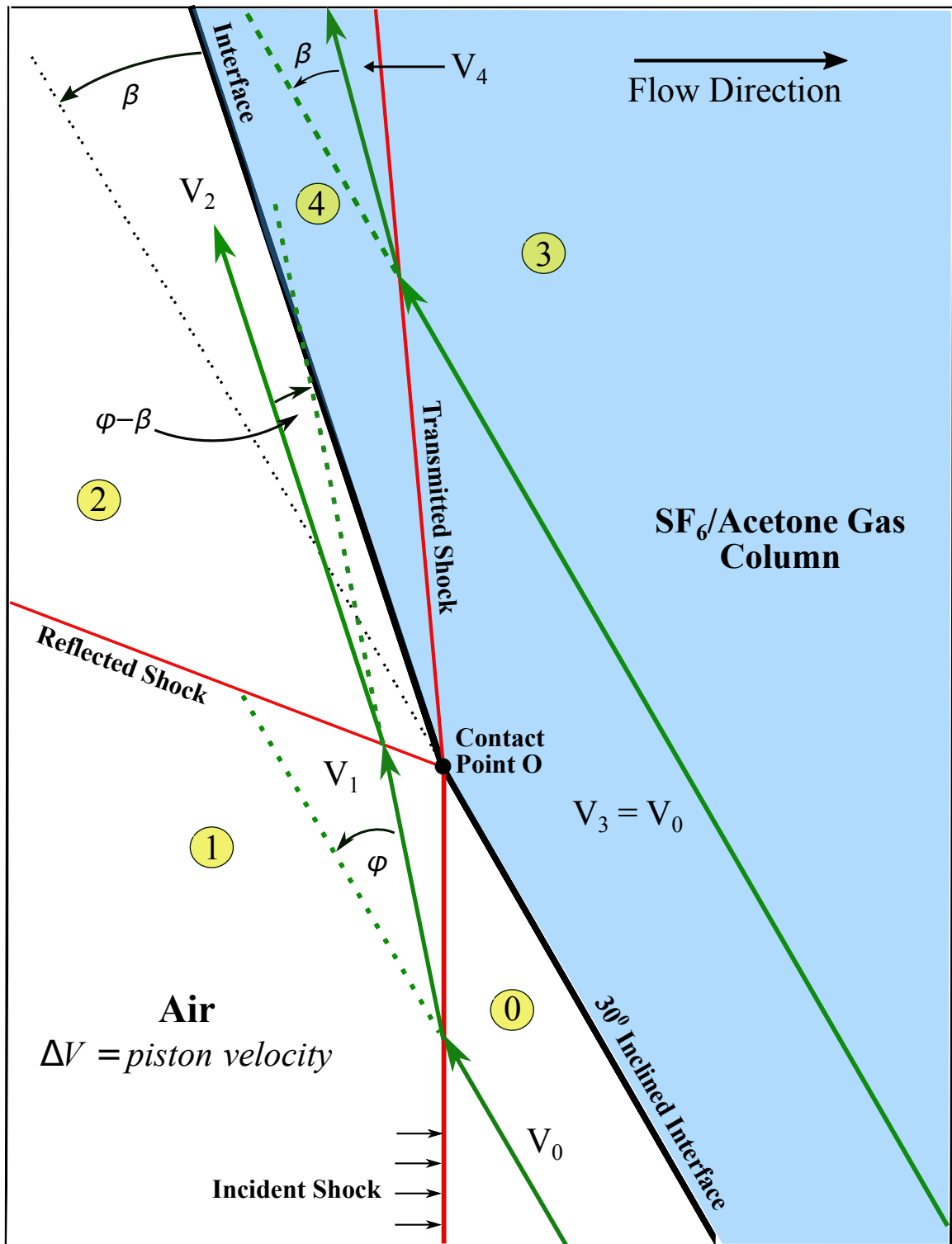
Figure 4.7: Schematic of the analytical approach developed by Sanjay Kumar of IIT in Kanpur, India. Changing from a laboratory reference frame to a contact point on the interface between the two gases.

scale, the flow near the leading edge of the tilted column can be regarded as two-dimensional [24]. The blue colored area, regions 3 and 4, corresponds to pure injected material (heavy gas) and the white area in regions 1 and 2 corresponds to pure air (light gas), moving at piston velocity $\Delta V$. Region 0 also contains pure air, but has not yet been accelerated by the shock wave. For the purposes of this analysis, region 0 is considered at rest.

When the shock impacts the heavy gas column, the diffuse interface is turned by some angle $\beta$, also referred to as the turning angle. At the same time, the shock creates two additional weaker shocks at the contact point. One of these shocks is reflected back into the light gas, which is moving at $\Delta V$. The other is a transmitted shock that propagates through the heavy gas column and is reflected back from the downstream edge of the column, creating a sort of pumping action, reverberating through the column. One theory [3] suggests this reverberating transmitted shock is responsible for the initial perturbations on the gaseous interface, which are then amplified in Kelvin-Helmholtz instability.

If the reference frame of this analysis is centered on the contact point O, it is possible to use simple trigonometric identities and compressible flow calculators, such as VuCalc [35] to determine the theoretical turning angle $\beta$. The turning angle is directly related to the shear layer along the upstream edge of the gas cylinder and to the compressed diameter of the cylinder ($D_c$) after shock impact [3]. The compressed diameter of the heavy gas cylinder, shown in Fig. 4.8, is the linear distance between the compressed leading edge of the column and the exit point of the shock on the trailing edge. It was assumed this variable would be useful in analyzing and predicting the length scale associated with the Kelvin-Helmholtz instabilities.

Once $V_0$, $V_1$, and $\phi$ have been calculated (see Fig.4.9), VuCalc is used to find other parameters of interest in each region, such as Mach number, pressure, temperature,
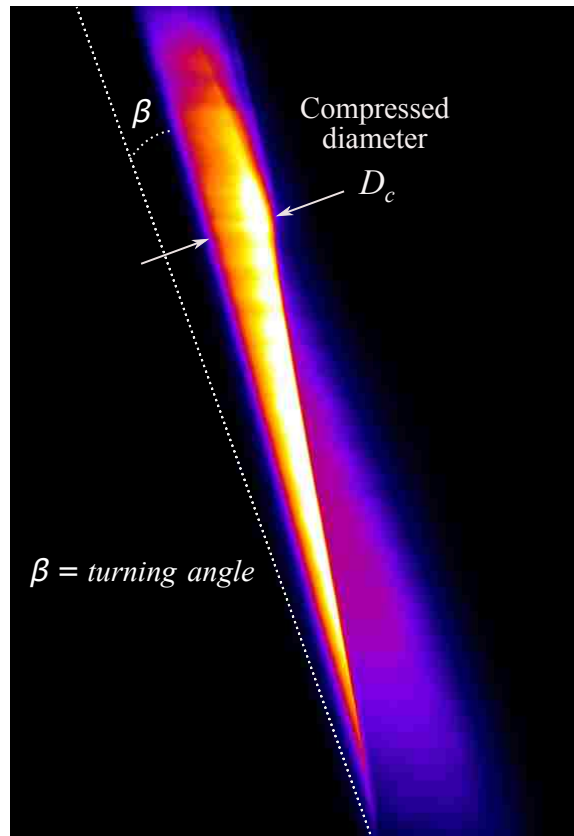
Figure 4.8: Image of a Mach = 1.7 shock wave impacting a column of acetone-infused $SF_6$. The length of the compressed diameter is shown along with a graphical interpretation of the turning angle $\beta$.

and density ratios. The turning angle is found by iterating over these parameters until the pressure ratios in regions 2 and 4 are equal. There exists no discontinuity between these regions. Therefore, the correct turning angle $\beta$ is one in which the static pressures in regions 2 and 4 are equal, regardless of the difference in densities between the air and post-shock injected material. The compressible flow calculator requires three inputs, the specific heat ratio of the gas in the region (1.4 for air and 1.1 for $SF_6$), the turning angle $\beta$ and the local Mach number with respect to the region of interest. The iterative variable here is $\beta$ and the local velocities in regions 2 and 4 ($\vec{V_2}$ and $\vec{V_4}$) are forced to remain parallel until the correct static pressure

is found. The theoretical turning angle $\beta$ for each Mach number and inclination angle $\theta$ are provided in Table 4.3. Preliminary measurements of turning angles in the experimental images agreed quite well with predicted values ($\leq 5\%$ error).



$$V_1^2 = V_p^2 + V_0^2 - 2V_p V_0 \cos\left(90 - \theta\right)$$

$$V_1 = \sqrt{V_p^2 + V_0^2 - 2V_p V_0 \cos\left(90 - \theta\right)}$$

$$V_0 = \frac{Ma_0}{\sin\left(\theta\right)}$$

$$\sin\left(\varphi\right) = \frac{V_p \sin\left(90 - \theta\right)}{V_1}$$
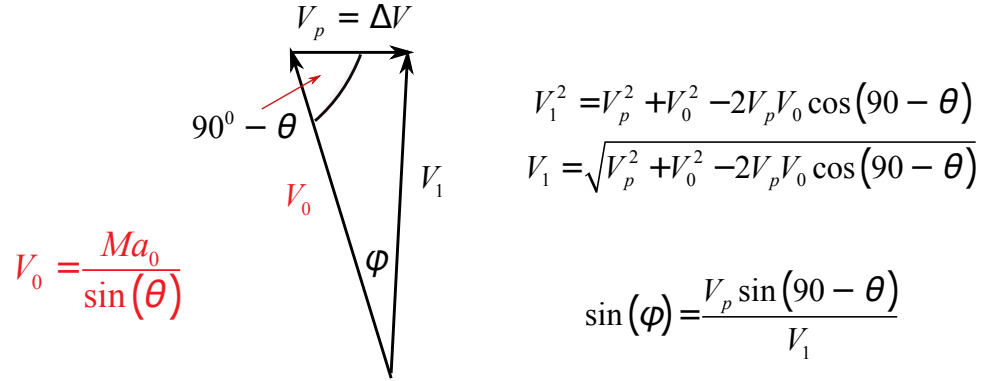
Figure 4.9: Depiction of the method used to find velocities $V_1$ and the angle $\phi$, which is the angle at which $V_0$ is turned after the normal shock has impacted. Velocity $V_1$ is the resulting velocity vector, turned by angle $\phi$.

Table 4.3: Turning angle $\beta$ according to Mach number for inclination angles $\theta = 30°$ and $\theta = 20°$, respectively.

| Mach Number | $\beta$ for $\theta = 30°$ | $\beta$ for $\theta = 20°$ |
|---|---|---|
| 1.13 | 3.275° | 2.000° |
| 1.45 | 8.000° | 5.770° |
| 1.70 | 10.00° | 7.050° |
| 2.00 | 11.75° | 8.110° |

The secondary variable of interest in the compressible flow calculations is the density ratio between regions 3 and 4 in the post-shock column (refer to Fig. 4.7). This value is used to calculate the theoretical compressed diameter $D_c$. Let the area and diameter of the pre-shocked column be $A_0$ and $D_0$, and $A_c$ and $D_c$ after the shock impact. Assume the density ratio $\rho_4/\rho_3$, determined after shock impact for the planar interface be equal to that of the compressed cylinder. This assumption,

combined with the law of conservation of mass leads to simple equations relating the compressed and uncompressed values describing the cylinder [24]:

$$\frac{A_c}{A_0} \approx \frac{\pi D_c{}^2/4}{\pi D_0{}^2/4} \approx \frac{1}{\rho_4/\rho_3} \qquad \longrightarrow \qquad \frac{D_c}{D_0} \approx \frac{1}{\sqrt{\rho_4/\rho_3}}$$

$$\implies D_c = \frac{D_0}{\sqrt{\rho_4/\rho_3}} \tag{4.2}$$

Tables 4.4 and 4.5 provide experimentally obtained measurements of the compressed diameter, along with predicted values of $D_c$ with respect to Mach number. The percent error between the experimental measurements and theoretical values is also provided. Table 4.4 corresponds to a $\theta = 20°$ angle of inclination, while Table 4.5 corresponds to $\theta = 30°$. Notice the sizable difference in error between the 20° and 30° data. This is most likely due to uncertainty in the experimental measurements. Depending on the intensity of the laser, the resolution of the camera, and any background noise in the exposure, the histogram for each image can be quite different. Therefore, finding the exact location of the shock exiting the cylinder is somewhat vague, especially at low Mach numbers.

Table 4.4: Experimental and theoretical compressed diameter with respect to Mach number and inclination angle $\theta = 20°$

| Mach Number | Experimental $D_c$ | Theoretical $D_c$ | Percent Error |
|---|---|---|---|
| 1.13 | 4.04 mm | 5.14 mm | 21.4% |
| 1.45 | 2.68 mm | 3.80 mm | 29.4% |
| 1.70 | 2.13 mm | 3.22 mm | 33.9% |
| 2.00 | 1.95 mm | 2.73 mm | 28.6% |

As stated previously, it was assumed the compressed diameter $D_c$ was the dominant length scale in these experiments. An effort was made to prove this assumption

Table 4.5: Experimental and theoretical compressed diameter with respect to Mach number and inclination angle $\theta = 30°$

| Mach Number | Experimental $D_c$ | Theoretical $D_c$ | Percent Error |
|:-----------:|:------------------:|:-----------------:|:-------------:|
| 1.13 | 5.06 mm | 5.30 mm | 4.60% |
| 1.45 | 4.25 mm | 4.09 mm | 3.91% |
| 1.70 | 3.46 mm | 3.39 mm | 2.09% |
| 2.00 | 3.12 mm | 2.76 mm | 16.7% |

by normalizing the experimentally measured wavelengths using $D_c$ and other relevant parameters, such as the Mach number, and the theoretical turning angle $\beta$. The goal here is to collapse the data from both inclination angles onto a single line or function that could describe the behavior of KHI wavelength with respect to Mach number. The normalization of KHI wavelength is as follows:

$$\lambda_c = \frac{\lambda}{D_c \tan(\beta)\sqrt{M}} \tag{4.3}$$

where $\lambda$ is the experimentally measured wavelength, normalized by the theoretical compressed diameter $D_c$, the tangent of the turning angle $\beta$, and the square root of the Mach number. This type of 1/2-power scaling of Mach number is important because 1/2-power scaling of Mach number occurs in supersonic planar turbulent wakes [36][37][38].

Figure 4.10 is normalized $\lambda_c$ versus Mach number for $\theta = 20°$ (red line), and $\theta = 30°$ (blue line) inclination angles. Horizontal error bars are $\pm$ one standard deviation in Mach number, while vertical error bars are $\pm$ one standard deviation in $\lambda$, normalized the same way as $\lambda_c$. Once again, the curve fits are simply used as a visual aid to show KHI wavelength behavior with respect to Mach number.

Granted, the curve fits in Fig. 4.10 are somewhat dissimilar. However, this is just the first attempt to characterize these instabilities as they are a relatively recent discovery in experiments of this type. Figure 4.10 does contain characteristics of
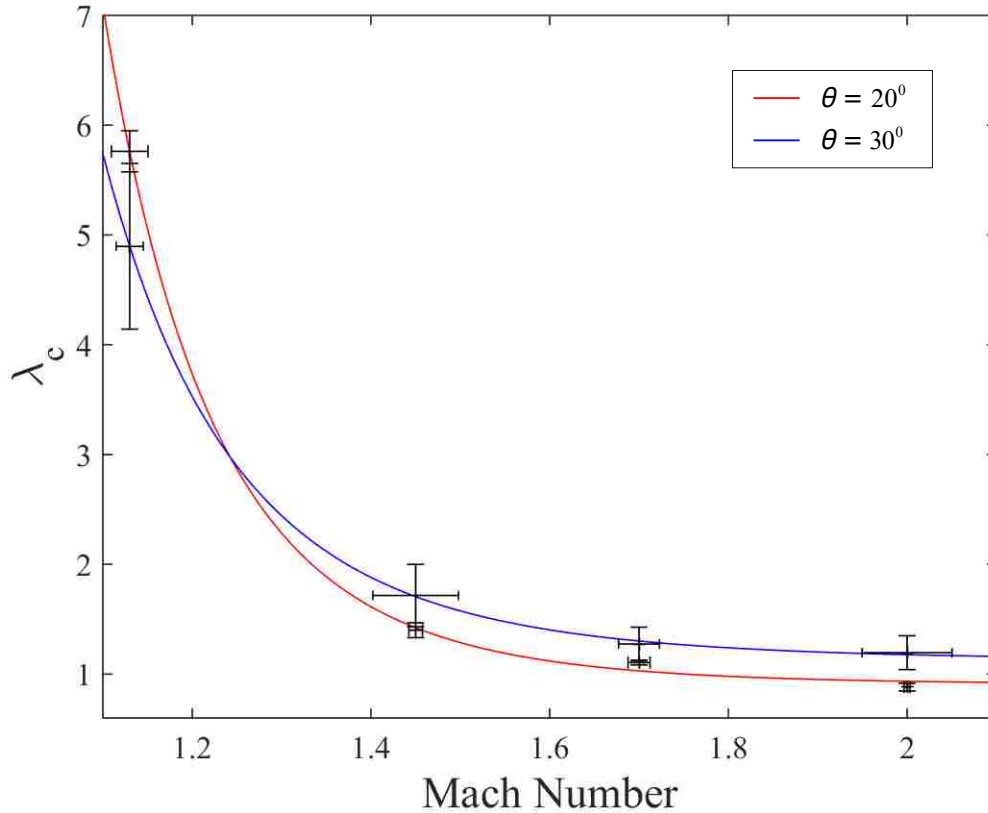
Figure 4.10: Normalized wavelength $\lambda_c$ versus Mach number for both inclination angles.

the flow itself, although they are theoretical approximations, and these characteristics were derived from properties of the two gases (light and heavy) after oblique shock interaction. However, one physical property was not accounted for during the theoretical analysis and that is the Atwood number of the experiment. Several studies [1][7][17][39], both numerical and experimental, have shown the development of Richtmyer-Meshkov instabilities depend on Atwood number. RMI are shock-driven instabilities whose evolution and development depend directly on the baroclinic term of the vorticity equation $\left( \vec{\nabla}\rho/\rho^2 \times \vec{\nabla}p \right)$. If the density of the injected gas changes, the magnitude of vorticity deposited on the column will also change. KHI are shear-

driven instabilities but Eqn. (3.12) is a function of the two fluid densities. Therefore, it might be wise to consider Atwood number variation in any future analyses.

# Chapter 5

# Conclusion

The evolution and development of KHI occurring in oblique shock interaction with a heavy gas column were analyzed and presented. Experimental and theoretical analysis of the instabilities was performed for two shock tube inclination angles, $\theta = 20°$ and $\theta = 30°$. Experiments were performed in the shock tube facility at the University of New Mexico Mechanical Engineering Department. Four representative Mach numbers were chosen for these experiments: $M = 1.13$, $M = 1.45$, $M = 1.70$, and $M = 2.00$. Vertical plane images of the shock-accelerated column were obtained with a high quantum efficiency (95%) Apogee U42 CCD camera. Images of the 30° angle of inclination were obtained before those at 20°. However, images taken at $\theta = 20°$ were obtained with much higher resolution than those at $\theta = 30°$. The reason for this is that as our understanding of the three-dimensional flow evolved, so did the nature of the experiments. Upgrades in equipment and more advanced data collection techniques were realized and implemented.

Time-resolved images of KHI provided insights into the development of the instabilities, including a better understanding of three-dimensional vorticity deposition on the heavy gas column, and the progression of KHI (and RMI in the centerline

plane), from shock impact to turbulent transition. Evolution of KHI begins with amplification of the initial perturbations on the diffuse interface into small wave-like structures. These structures grow in amplitude and eventually form large co-rotating billows along the entire vertical length of the leading edge of the column. These billows grow in amplitude and quickly combine, effectively doubling in wavelength, before mixing with surrounding material and transitioning to fully turbulent flow. Wave-like structures also present on the trailing edge of the high-density region (for reference see Fig. 4.2). However, their development is ambiguous at best considering their size; an order of magnitude smaller than the KHI on the leading edge. This is likely due shock focusing on the trailing edge disrupting vortex formation in the vertical plane. It was found that these instabilities are dependent on two variables: Mach number and inclination angle $\theta$. The instabilities decrease in wavelength (and amplitude) with increasing Mach number. An opposite trend was found for $\theta$ dependence: wavelength decreases as $\theta$ decreases. The limiting case is $\theta = 0°$, where no instabilities form on the leading edge of the column. Because no shear along the horizontal interface, shear-driven KHI cannot develop.

Quantitative analysis was also performed of the images, providing confirmation of Mach number and $\theta$ dependence. For an angle of $\theta = 30°$, wavelengths ranged between 1.00 mm for $M = 1.13$ to 1.60 mm for $M = 2.00$. For the $\theta = 20°$ case, wavelengths ranged from 0.50 mm for $M = 1.13$ and 1.10 mm for $M = 2.00$. A theoretical approach, proposed by Sanjay Kumar of IITK, was developed in an effort to quantify shear velocities along the interface between air traveling down the leading edge of the column, and the injected material (acetone-infused $SF_6$). According to the theoretical model, calculations of shear velocities approach infinity as $\theta \longrightarrow 0$. Therefore, the analysis could not accurately predict the magnitude of the shear velocities. However, the analysis did provide a prediction of the compressed diameter of the column, $D_c$, and turning angle $\beta$. These quantities agreed well with experimental measurements and were used to non-dimensionalize KHI wavelength

with respect to Mach number in order to collapse the data into a single function that describes KHI behavior, independent of inclination angle $\theta$. This information could be invaluable to future analyses of KHI developing from shock interactions, and provide a basis for predicting their behavior using numerical techniques.

Future studies will include measurements of velocity field associated with the vertical-plane shear layer, using image correlation velocimetry [40], measurements of line stretching [41], and fractal properties [42] of the scalar field.

# References

[1] M. Anderson, P. Vorobieff, C. R. Truman, C. Corbin, G. Kuehner, P. Wayne, J. Conroy, R. White, and S. Kumar, "An experimental and numerical study of shock interaction with a gas column seeded with droplets," *Shock Waves*, vol. 25, pp. 107–125, March 2015.

[2] P. Wayne, D. Olmstead, P. Vorobieff, C. R. Truman, and S. Kumar, "Oblique shock interaction with a cylindrical density interface," *Computational Methods of Multiphase Flow VIII*, vol. 89, pp. 161–169, 2015.

[3] D. Olmstead, *Oblique shock wave effects on an impulsively accelerated heavy gas column.* Ph. D. thesis, University of New Mexico, 2015.

[4] R. Richtmyer, "Taylor instability in shock acceleration of compressible fluids," Tech. Rep. LA-1914, Scientific Laboratory of the University of California, Los Alamos, New Mexico, July 1954.

[5] E. E. Meshkov, "Instability of the interface of two gases accelerated by a shock-wave," *Izv. AN SSSR, Mekh. Zhidk. Gaza*, vol. 4, no. 5, pp. 151–157, 1969.

[6] C. Niederhaus, *Experiments on the Richtmyer-Meshkov instability of incompressible fluids.* Ph.D. thesis, University of Arizona, 2000.

[7] M. J. Anderson, *Oblique shock interactions with perturbed density interfaces.* Ph.D. thesis, University of New Mexico, 2011.

[8] O. Darrigol, *Worlds of Flow: A history of hydrodynamics from the Bernoullis to Prandtl.* New York: Oxford University Press, 2005.

[9] O. Darrigol, "Empirical challenges and concept formation in the history of hydrodynamics," *Centaurus*, vol. 50, no. 3, pp. 214–232, 2008.

*References*

[10] K. Moffatt, "Vortex dynamics: The legacy of Helmholtz and Kelvin," in *IU-TAM Symposium on Hamiltonian Dynamics, Vortex Structures, Turbulence* (A. Borisov, V. Kozlov, I. Mamaev, and M. Sokolovskiy, eds.), vol. 6 of *IU-TAM Bookseries*, pp. 1–10, Springer Netherlands, 2008.

[11] H. Sharlin, "William Thomson, Baron Kelvin." `http://www.britannica.com/EBchecked/topic/314541/William-Thomson-Baron-Kelvin/13895/Early-life`. Accessed: 2015 - 03 - 03.

[12] D. Ryu, T. Jones, and A. Frank, "The magnetohydrodynamic Kelvin-Helmholtz instability: a three-dimensional study of nonlinear evolution," *The Astrophysical Journal*, vol. 545, no. 1, pp. 475–493, 2000.

[13] W. Smyth and K. Winters, "Turbulence and mixing in Holmboe waves," *Journal of Physical Oceanography*, vol. 33, pp. 694–711, 2002.

[14] R. White, "Oblique shock wave interactions with gas cylinder interfaces," Master's thesis, University of New Mexico, 2012.

[15] P. Vorobieff, M. Anderson, J. Conroy, R. White, and C. R. Truman, "Vortex formation in a shock-accelerated gas induced by particle seeding.," *Physical Review Letters*, vol. 106, p. 184503, 2011.

[16] P. Vorobieff, M. Anderson, J. Conroy, R. White, C. Truman, and S. Kumar, "Analogues of Rayleigh-Taylor and Richtmyer-Meshkov instabilities in flows with nonuniform particle and droplet seeding," *Computational Methods in Multiphase Flow VI*, vol. 70, pp. 17–28, 2011.

[17] M. Anderson, P. Vorobieff, S. Kumar, J. Conroy, R. White, C. Needham, and C. Truman, "Numerical simulation of a shock-accelerated multiphase fluid interface," in *28th International Symposium on Shock Waves* (K. Kontis, ed.), pp. 923–929, Springer Berlin Heidelberg, 2012.

[18] S. Kumar, G. Orlicz, C. Tomkins, C. Goodenough, K. Prestridge, P. Vorobieff, and R. Benjamin, "Stretching of material lines in shock-accelerated gaseous flows," *Physics of Fluids*, vol. 17, p. 082107, Aug. 2005.

[19] T. Tran, Y. Kochar, and J. Seitzman, "Measurement of liquid acetone fluorescence and phosphorescence for two-phase imaging," No. 2005-0827, (Reno, NV), 43rd Aerospace Sciences Meeting and Exhibit, 2005.

[20] M. C. Thurber, *Acetone laser-induced fluorescence for temperature and multiparameter imaging in gaseous flows*. PhD thesis, Stanford University, California, 1999.

*References*

[21] W. Ure, "The vapor pressure of acetone at low temperatures," Master's thesis, University of British Colombia, Canada, 1924.

[22] J. Yoo, "Effects of Atwood number on Kelvin-Helmholtz instabilities formed from oblique shock interaction with a heavy gas column," *AIAA Region IV Student Conference*, 2015.

[23] A. Liquide. `http://encyclopedia.airliquide.com/Encyclopedia.asp?GasID=34#GeneralData`. Accessed: 2015-04-06.

[24] D. Olmstead, P. Wayne, S. Kumar, C. R. Truman, and P. Vorobieff, "Experimental study of shock accelerated inclined heavy gas cylinder," *Journal of Fluid Mechanics*, 2015. Submitted.

[25] B. Munson, T. Okiishi, W. Huebsch, and A. Rothmayer, *Fundamentals of Fluid Mechanics*, ch. 1. Hoboken, New Jersey: John Wiley and Sons, 7th ed., 2013.

[26] Merriam-Webster. `http://www.merriam-webster.com/dictionary/hydrodynamics`. Accessed:2015-07-05.

[27] I. G. Currie, *Fundamental Mechanics of Fluids*, ch. 3-6. Boca Raton, Florida: CRC Press, Taylor and Francis Group, 4th ed., 2013.

[28] L. Milne-Thomson, *Theoretical Hydrodynamics*, ch. 2. London, England: MacMillan and Co., 1938.

[29] R. Chevray and J. Mathieu, *Topics in Fluid Mechanics*, ch. 3. New York, NY: Cambridge University Press, 1993.

[30] J. A. Liggett, *Fluid Mechanics*. Columbus, OH: McGraw-Hill, 1994.

[31] A. Hogg and G. Ivey, "The Kelvin-Helmholtz to Holmboe instability transition in stratified exchange flows," *Journal of Fluid Mechanics*, vol. 477, pp. 339–362, 2003.

[32] U. of Wisconsin Madison, "WiSTL Wisconsin Shock Tube Laboratory." `http://silver.neep.wisc.edu/~shock/tools/gdcalc.html`. Accessed: 2015-05-15.

[33] B. Motl, J. Oakley, D. Ranjan, C. Weber, M. Anderson, and R. Bonazza, "Experimental validation of a Richtmyer-Meshkov scaling law over large density ratio and shock strength ranges," *Physics of Fluids*, vol. 21, p. 126102, Dec. 2009.

*References*

[34] J. A. McFarland, J. A. Greenough, and D. Ranjan, "Simulations and analysis of the reshocked inclined interface Richtmyer-Meshkov instability for linear and nonlinear interface perturbations," *Journal of Fluids Engineering*, vol. 136, p. 071203, May 2014.

[35] R. Carmichael, "vuCalc-A Compressible Flow Calculator." http://www.pdas.com/vucalc.html#oblq, Feb. 2013.

[36] A. Wohler, K. Mohri, and B. Weigand, "Flow structures in subsonic-to-supersonic mixing processes using different injector geometries," in *4th European Conference for Aerospace Sciences* (L. DeLuca, C. Bonnal, O. Haidn, and S. Frolov, eds.), (St. Petersburg, Russia).

[37] M. Nakagawa and W. Dahm, "Compressibility effects on entrainment and mixing in supersonic planar turbulent wakes," in *30th AIAA Fluid Dynamics Conference*, no. AIAA 99-3582, (Reno, NV), 1999.

[38] M. Nakagawa and W. Dahm, "Mach number effects on entrainment and mixing in supersonic planar turbulent wakes," in *38th Aerospace Sciences Meeting and Exhibit*, no. AIAA 2000-0664, (Reno, NV), 2000.

[39] J. McFarland, J. Greenough, and D. Ranjan, "Computational parametric study of a Richtmyer-Meshkov instability for an inclined interface," *Physical Review E*, vol. 84, no. 1, 2011.

[40] P. Tokumaru and P. Dimotakis, "Image correlation velocimetry," *Experiments in Fluids*, vol. 19, no. 1, pp. 1–15, 1995.

[41] S. Kumar, G. Orlicz, C. Tomkins, C. Goodenough, K. Prestridge, P. Vorobieff, and R. Benjamin, "Stretching of material lines in shock-accelerated gaseous flows," *Physics of Fluids (1994-present)*, vol. 17, no. 8, p. 082107, 2005.

[42] P. Vorobieff, P. M. Rightley, and R. F. Benjamin, "Shock-driven gas curtain: fractal dimension evolution in transition to turbulence," *Physica D: Nonlinear Phenomena*, vol. 133, no. 1, pp. 469–476, 1999.